Nano Research
2023, 16(8): 10881–10889

ISSN 1998-0124 CN 11-5974/O4
https://doi.org/10.1007/s12274-023-5953-y

Research Article

# Bimetallic clusters confined inside silicalite-1 for stable propane dehydrogenation

Xueer Wei[1,§], Jiawei Cheng[1,§], Yubing Li[1], Kang Cheng[1,2] (✉), Fanfei Sun[3,4] (✉), Qinghong Zhang[1] (✉), and Ye Wang[1,2]

[1] *State Key Laboratory of Physical Chemistry of Solid Surfaces, Collaborative Innovation Center of Chemistry for Energy Materials, College of Chemistry and Chemical Engineering, Xiamen University, Xiamen 361005, China*
[2] *Innovation Laboratory for Sciences and Technologies of Energy Materials of Fujian Province (IKKEM), Xiamen 361005, China*
[3] *Shanghai Synchrotron Radiation Facility, Shanghai Advanced Research Institute, Chinese Academy of Sciences, Shanghai 201800, China*
[4] *Shanghai Institute of Applied Physics, Chinese Academy of Sciences, Shanghai 201204, China*
[§] *Xueer Wei and Jiawei Cheng contributed equally to this work.*



**Received:** 20 April 2023 / **Revised:** 11 June 2023 / **Accepted:** 23 June 2023

## ABSTRACT

The noble metal-based bimetallic clusters with high atom utilization and surface energy have been widely applied in heterogeneous catalysis, but the stabilization of these metastable clusters in harsh reaction conditions is quite challenging. Herein, we synthesize a series of Pt-, Pd-, and Ru-based clusters promoted by a second non-noble metal (Zn, Cu, Sn, and Fe), which are confined inside silicalite-1 (pure silica, S-1) crystals by a ligand-protected method. The second metal could well stabilize and disperse the noble atoms inside the rigid S-1 zeolites via Si–O–M bonds, thus enabling to lower the usage of expensive noble metals in catalysts. The as-synthesized bimetallic catalysts exhibited excellent performance in non-oxidative propane dehydrogenation (PDH) reaction, which is typically operated above 500 °C. The PtZn@S-1, PtCu@S-1, and PtSn@S-1 with only a ~ 0.17 wt.% Pt loading offer a significant enhancement in PDH performance compared with the conventional $PtSn/Al_2O_3$ catalyst with a 0.5 wt.% Pt loading prepared by impregnation method. Notably, the PtSn@S-1 provides a propane conversion of 45% with a 99% propylene selectivity at 550 °C, close to the thermodynamic equilibrium. Furthermore, the PtSn@S-1 exhibits excellent stability during 300 h on stream and high tolerance to regeneration by a simple calcination step.

## KEYWORDS

zeolite, noble metal, bimetallic, confinement, alkane conversion

## 1 Introduction

Supported noble metal catalysts have been widely applied in a variety of key chemical technologies, such as selective hydrogenation, biomass valorization, three-way catalysts, and light alkane dehydrogenation [1–4]. Considering the atom economy, a higher dispersion or smaller particle size can effectively improve the utilization of expensive noble metals. With this regard, a series of single-atom catalysts (SACs) and fully exposed cluster catalysts have been designed and developed to enhance the dispersion of active metals [5–7]. However, the sintering of metal species by Ostwald ripening or particle migration mechanisms on the support surface is often inevitable under harsh pretreatment, reaction, and regeneration conditions [8–11]. This phenomenon not only causes a reduction in catalyst activity and stability but may also catalyze the formation of the by-products, thus the stabilization of highly dispersed metal sites under complex working conditions is the frontier of heterogeneous catalysis [12–14].

Zeolites are microporous materials with well-defined structures, and their hydrothermal stability can be up to 850 °C without a significant drop in crystallinity and surface area [15–17]. In heterogeneous catalysis, zeolites are often combined with noble metals for constructing bifunctional catalysts or confining active metal sites in the micropore channels [18–20]. It is noteworthy that the diffusion of tightly fitting reactant molecules inside zeolite micropores follows a configurational diffusion mechanism, thus the diffusion becomes a rate-determining step [21, 22]. Most successful examples of metal@zeolite in catalysis are based on the transformation of small molecules, such as CO, $CO_2$, $NO_x$, $CH_4$, and light alkanes [23–26]. On the other hand, noble metals are usually modified by a second non-noble metal to tune the microenvironment of active sites and decrease their loading for catalysis [27–29]. In the recent past, the confinement of bimetallic sites within the zeolite crystals or micropores has been confirmed as an effective strategy to boost catalytic performances, especially for high-temperature reactions [13, 19, 30]. Accordingly, several synthesis protocols for metal@zeolite materials have been explored, including ion exchange, the introduction of a metal complex during hydrothermal synthesis, re-crystallization, and the grafting of the metal species onto the framework defects [31–34].

Propane dehydrogenation (PDH) is an on-purpose propylene production technology that has received extensive attention driven

Address correspondence to Kang Cheng, kangcheng@xmu.edu.cn; Fanfei Sun, sunfanfei@sinap.ac.cn; Qinghong Zhang, zhangqh@xmu.edu.cn

by the shale gas revolution [35–38]. PDH is a highly endothermic reaction and requires high reaction temperatures, typically higher than 500 °C. The harsh reaction conditions often catalyze the side reactions including cracking, deep dehydrogenation of propane, and the formation of complex coking deposition species, and also accelerate the sintering and agglomeration of active centers leading to rapid catalyst deactivation [39–41]. Noble-based catalysts are preferentially employed for PDH reactions due to their excellent ability in C–H bond activation [42], among which Pt-based catalysts promoted by Sn, Zn, and Ga exhibit superior performances [39–41]. Nevertheless, to extend the catalyst's lifetime, periodic calcination, oxychlorination, and reduction must be conducted, which increases energy consumption and carbon emission [43]. To alleviate this problem, a series of Pt-based bimetallic clusters confined inside all silica zeolites have been successfully developed to improve the stability of PDH reactions [44–46]. Besides, PDH catalysts with Pd, Ru, and Ir as the main active metals were also developed and exhibited comparable performance as Pt-based catalysts [47–49]. However, to maintain the PDH performance, the noble metal loadings of these catalysts are typically above 0.5 wt.%, which is much higher than 0.3 wt.% of the industrial $PtSn/Al_2O_3$ catalysts [50]. Exploring noble metal-based catalysts with low loadings and high atom utilization for stable PDH reactions is still a challenging task.

In this work, we synthesized a series of bimetallic cluster catalysts confined inside silicalite-1 (S-1) crystals by a universal ligand-protected strategy, with high dispersion of noble metals modified by a second non-noble metal (Sn, Zn, Cu, and Fe). These non-noble metals have been frequently applied as structural or electronic promoters for noble mental in the catalytic conversion of light alkanes [29, 31]. The catalysts were unequivocally visualized by transmission electron microscopy (TEM) assisted by ultramicrotomy and spherical aberration correction to evaluate the metal location and distribution. The bimetallic clusters smaller than 2 nm could be well stabilized inside the S-1 crystals by Si–O–M bonds even at 550 °C. Owing to the high dispersion of noble metals, the optimum PtZn@S-1, PtCu@S-1, and PtSn@S-1 with only ~ 0.17 wt.% of Pt loading could maintain propane conversion levels close to the thermodynamic equilibrium and the propylene selectivity as high as 99%.

## 2 Experimental

### 2.1 Chemicals

Platinum dichloride ($PtCl_2$), palladium dichloride ($PdCl_2$), ruthenium trichloride ($RuCl_3$), chloroplatinic acid hydrate ($H_2PtCl_6{\cdot}6H_2O$), tin tetrachloride pentahydrate ($SnCl_4{\cdot}5H_2O$), and gallium nitrate ($Ga(NO_3)_3{\cdot}xH_2O$) were purchased from Aladdin Reagent. Zinc acetate ($C_4H_6O_4Zn{\cdot}2H_2O$), ethylenediamine (EDA) ferric nitrate ($Fe(NO_3)_3{\cdot}9H_2O$), bismuth chloride ($BiCl_3$), and ethyl orthosilicate (TEOS) were purchased from Sinopharm Chemical Reagent Co., Ltd. Copper acetate ($Cu(CH_3COO)_2{\cdot}H_2O$), lanthanum acetate ($La(CH_3COO)_3{\cdot}3H_2O$), cadmium acetate ($Cd(CH_3COO)_2{\cdot}2H_2O$), and tetrapropylammonium hydroxide (TPAOH, 40%) were purchased from Energy Chemical Reagent. Propane ($C_3H_8$, 99.9%) was purchased from Dalian Special Gas Co., Ltd. Glassware was provided by Xiamen University Glassware Workshop.

### 2.2 Catalyst preparation

S-1 was synthesized by a hydrothermal method with ligand protection. Typically, 8.13 g TPAOH solution (40 wt.%) was mixed with 15 g of deionized water and stirred for 15 min at room temperature. Then, 8.32 g TEOS was added into the solution, stirred for 6 h, and transferred to a 100 mL Teflon-lined stainless steel autoclave. Hydrothermal crystallization was conducted under static conditions at 170 °C for 3 days. The solid products were collected after washing, centrifugation, and drying overnight at 80 °C. The organic template was removed by calcination at 550 °C for 6 h. The metal-EDA complexes were prepared by dissolving an appropriate amount of metal compound into an aqueous solution containing ethylenediamine. Then the mixture was stirred until completely dissolved. The cluster@ S-1 was synthesized by a modified hydrothermal method. Taking PtM@S-1 as an example, typically, 8.13 g TPAOH solution (40 wt.%) was mixed with a certain amount of deionized water, and then an appropriate amount of Pt complexes in the solution were added and stirred for 10 min at room temperature. Then, 8.32 g TEOS was added to the mixture dropwise and stirred for 6 h, after which a certain amount of promoter-EDA complexes were added into the mixture and stirred for another 30 min. The obtained precursor was transferred to a 100 mL Teflon-lined autoclave and crystallized at 170 °C for 3 days. The solid products were collected after washing, centrifuging, and drying at 80 °C overnight. Finally, the $Pt_xM_y$@S-1 was obtained by reduction at 400 °C for 2 h under $H_2$ flow ($x$ and $y$ denote the metal weight percentage (based on $SiO_2$) introduced into hydrothermal solutions). PtZn/S-1 and $PtSn/Al_2O_3$ were prepared by a traditional impregnation method.

### 2.3 Catalyst characterizations

X-ray powder diffraction (XRD) was measured on a Smart Lab-SE physical X-ray diffractometer with Cu K$\alpha$ radiation ($\lambda$ = 0.15406 nm) X-ray source (40 kV and 30 mA). The porosity of the sample was determined on the Micromeritics Tri-Star II 3020 surface area analyzer. Samples are treated under vacuum at 250 °C for 2 h before $N_2$ adsorption. CO Fourier-transform infrared (CO-FTIR) spectroscopy was analyzed on a Nicolet 6700 spectrometer equipped with an MCT detector. Typically, 10 mg sample was pressed into a self-supporting wafer and placed in an *in situ* infrared (IR) cell, then heated to 550 °C and reduced by a 10 vol.% $H_2$/Ar gas for 1 h. After cooling to room temperature, a 10 vol.% CO/Ar gas was introduced for 1 h. The CO adsorption spectra were recorded after purification of the sample with flow Ar for 1 h. Metal content was analyzed by an X-ray fluorescence (XRF) spectroscopy on a Panalytical Axios-Petro XRF instrument.

X-ray photoelectron spectroscopy (XPS) analysis was carried out using a Quantum 2000 Scanning ESCA Microprobe with Al K$\alpha$ radiation (1846.6 eV) as the X-ray source. The binding energy was calibrated using the C 1s photoelectron peak of 284.6 eV. Scanning electron microscopy (SEM) was performed on a Hitachi S-4800 at 15 kV. High-resolution TEM (HRTEM) and the corresponding energy-dispersive X-ray (EDX) mapping analysis were obtained on a Phillips Analytical FEI Tecnai 20 electron microscope with an accelerating voltage of 200 kV. Aberration-corrected high-angle annular darkfield scanning transmission electron microscopy (AC-HAADF-STEM) was performed on the JEM-ARM200F.

X-ray absorption fine structure (XAFS) measurements were performed at the BL14W1 in Shanghai Synchrotron Radiation Facility (SSRF). The electron beam energy was 3.5 GeV and the stored current was 200 mA (top-up). A 38-pole wiggler with a maximum magnetic field of 1.2 T inserted in the straight section of the storage ring was used. XAFS data were collected using a fixed-exit double-crystal Si (111) monochromator. The fluorescence signal was collected by an silicon drift detector (SDD) and the transmission signal was collected by gas ionization chambers. The energy was calibrated using corresponding metal

foils. The photon flux at the sample position was 2.6 × $10^{12}$ photons per second. The raw data analysis was performed using the IFEFFIT software package according to the standard data analysis procedures [51]. The spectra were calibrated, averaged, pre-edge background subtracted, and post-edge normalized using the Athena program in the IFEFFIT software package. The weight of Fourier transformation was 3 for Zn K-edge and Cu K-edge extended X-ray absorption fine structure (EXAFS) oscillations. The weight of Fourier transformation was 2 for Pt $L_3$-edge and Sn K-edge EXAFS oscillations. From *K* space to *R* space was performed to obtain a radial distribution function. And data fitting was done by the Artemis program in IFEFFIT.

### 2.4 Catalyst evaluation

The PDH performance was evaluated in an atmospheric fixed-bed tubular quartz reactor with an inner diameter of 10 mm designed and built by Xiamen Hande Precision Industry Co., Ltd. Typically, 0.3 g catalyst was diluted with 1 g quartz sand and loaded into the reactor, after which the reactor was heated to 550 °C under $N_2$ flow of 30 mL·min$^{-1}$. The gas was then switched to flow $H_2$ with 20 mL·min$^{-1}$ for 1 h at 550 °C. The PDH was initiated by switching flow $H_2$ to a $C_3H_8/N_2$ (vol/vol = 1:3) flow with 40 mL·min$^{-1}$ at 550 °C and the weight hourly space velocity at this condition is 3.6 h$^{-1}$.

The products were analyzed by an online gas chromatograph (Ruimin GC-2060, Shanghai), equipped with a hydrogen flame ionization detector (FID) and a thermal conductivity detector (TCD) connected to the Rt-Q-Bond capillary column. Assuming that all gaseous hydrocarbon products could be detected and analyzed by FID and $H_2/N_2$ could be detected by TCD, the propane dehydrogenation performance was calculated based on a normalization method. Propane conversion and product selectivity were calculated by Eqs. (1)–(3)

$$\text{Select. } n\ (\%) = A_n / A_{\text{product}} \times 100\% \quad (1)$$

$$\text{Conv. } C_3H_8\ (\%) = A_{\text{product}} / (A_{\text{product}} + A_{C_3H_8}) \times 100\% \quad (2)$$

$$\text{Yield } n\ (\%) = \text{Select. } n \times \text{Conv.} C_3H_8 \times 100\% \quad (3)$$

where $n$ and $A$ represent each hydrocarbon product and their corresponding FID peak area, respectively. The carbon balance is better than 98%.

## 3 Results and discussion

### 3.1 Catalyst synthesis and characterization

The synthetic procedure for metal@S-1 catalysts is illustrated in Fig. 1(a). The metal complexes were prepared by mixing metal salts and EDA via electrostatic interactions and then introduced into the initial gel containing the templating agent ($TPA^+$) and TEOS. The *in situ* encapsulation of the metal complexes in zeolites was completed during the crystallization. The noble metal feeding in the hydrothermal step for this series of catalysts was 0.75 wt.% and the loading of the second metal was preoptimized for PDH reactions. The metal@S-1 catalysts were obtained after a direct reduction step and denoted as fresh catalysts. The sharp and strong XRD peaks at $2\theta$ = 7.9°, 8.9°, 23.1°, 23.9°, and 24.4° over $Pt_{0.75}Zn_{1.0}$@S-1, $Pd_{0.75}Zn_{1.0}$@S-1, and $Ru_{0.75}Zn_{1.0}$@S-1 indicate the successful synthesis of S-1 with MFI topology (Fig. 1(b)). No characteristic diffraction peaks belonging to metal species or their alloys were observed, suggesting a high dispersion of metal species. A similar trend was also observed over other metal@S-1 catalysts (Fig. S1 in the Electronic Supplementary Material (ESM)).

The SEM imaging suggests that the $Pt_{0.75}Zn_{1.0}$@S-1 exhibited a regular hexagonal cubic shape with an average size of ~ 250 nm, and no amorphous phases were observed, evidencing the high crystallinity of as-synthesized catalysts (Fig. 1(c)). The high-resolution TEM imaging shows that the metal clusters with a small size of ~ 1.5 nm were highly dispersed in zeolites (Fig. 1(d)), consistent with the XRD analysis that no characteristic diffraction peaks of metal (oxide) were detected. The Pd- and Ru-based bimetallic clusters confined inside S-1 crystals could also be synthesized by this ligand-protected method (Figs. 1(e) and 1(f), and Fig. S2 in the ESM). The crystal shape, metal particle size, and metal distribution were not influenced by the metal types, suggesting the generality of this synthesis method.

Since normal TEM imaging only provides a 2-dimensional projection of 3-dimensional material and the crystal size of S-1 was too thick for accelerated electrons, the realistic location of

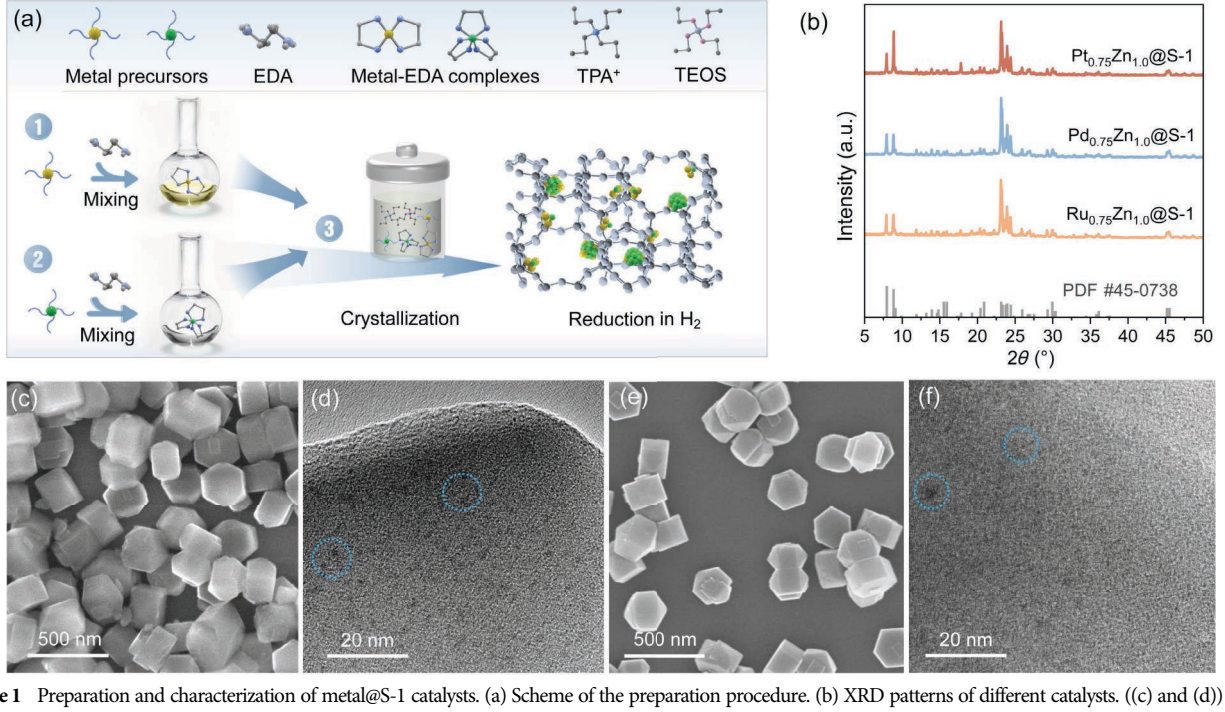


**Figure 1** Preparation and characterization of metal@S-1 catalysts. (a) Scheme of the preparation procedure. (b) XRD patterns of different catalysts. ((c) and (d)) SEM and TEM images of $Pt_{0.75}Zn_{1.0}$@S-1. ((e) and (f)) SEM and TEM images of $Pd_{0.75}Zn_{1.0}$@S-1.

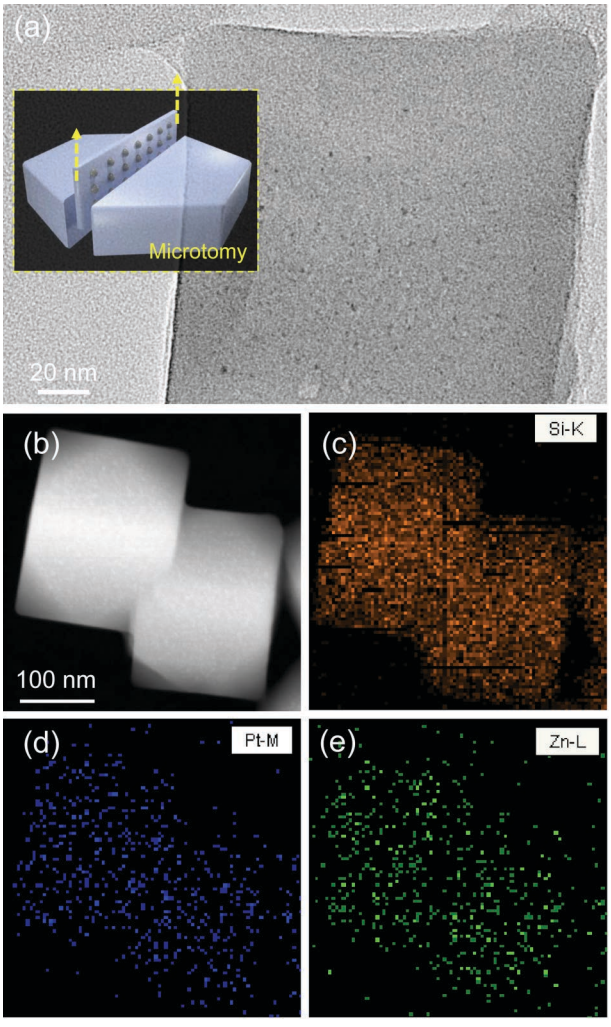


**Figure 2** The location and distribution of PtZn clusters of fresh $Pt_{0.75}Zn_{1.0}$@S-1. (a) TEM and (b) HAADF-STEM images. ((c)–(e)) EDX mapping.

metal clusters in the metal-zeolite catalysts can be ambiguous [52]. To explore the location and distribution of the bimetallic clusters in the S-1 crystal, we cut the PtZn@S-1 catalyst into 70 nm-thick sections using ultramicrotomy [22], which was then visualized by TEM. The TEM image with better contrast demonstrates that the PtZn clusters were indeed encapsulated within the S-1 crystals (Fig. 2(a)). It is noteworthy that the sizes of these clusters (~ 1.5 nm) are much larger than the micropore sizes of S-1 (0.55 nm), indicating a collapse of neighboring micropores upon particle growth [53]. In other words, the metal clusters were confined in zeolite crystals, not micropore channels [22]. One may think that micropores of S-1 would be blocked by PtM clusters, but the $N_2$-physisorption suggests that the porosity of S-1 was not significantly influenced by confining PtM clusters as compared with the pristine S-1 (Table S1 in the ESM). The MFI has a 3-dimensional pore structure, which makes the micropore volume easily accessible for most small molecules from every direction. The encapsulation structure was also evidenced over PtCu@S-1 and PtSn@S-1 (Fig. S3 in the ESM). Furthermore, the HAADF-STEM image and EDX mapping confirmed the high dispersion of PtZn clusters and the uniform element distribution along zeolite crystals (Figs. 2(b)–2(e)). The affinity between Pt and the second metal may provide synergy in their application for catalysis.

Pt-based metal@S-1 catalysts with a low Pt dosage of 0.2 wt.% were carefully characterized by AC-HADDF-STEM imaging (Fig. 3). By analyzing more than 200 clusters, more than 95% of clusters were in the range of 0.5–1.9 nm for both $Pt_{0.2}Zn_{0.8}$@S-1 and $Pt_{0.2}Cu_{0.8}$@S-1 (Figs. 3(a) and 3(b)). Interestingly, most clusters were located inside the inner region of S-1 crystals, while the shell of S-1 was almost empty of metal clusters. Besides, the XPS spectra also reveal that no Pt species on the surface layers of metal@S-1 catalysts (Fig. S4 in the ESM). This spatial organization might prevent the sintering of metal clusters to a maximum extent.

No isolated single-atom Pt was observed over $Pt_{0.2}Zn_{0.8}$@S-1 within the resolution of the electron microscope (Fig. 3(c)). According to the Z-contrast mechanism, the AC-HADDF-STEM imaging can distinguish Pt from promoters like Zn and Cu. The close-up images of the intensity profiles indicate the single cluster was composed of both Pt and Zn atoms, suggesting the formation of bimetallic phases. However, both Pt clusters and SACs were observed over fresh $Pt_{0.2}Cu_{0.8}$@S-1 (Fig. 3(d)), suggesting that the dispersion of Pt in S-1 crystals would be impacted by the type of second metal. Most metal clusters were mainly composed of Pt and Cu over $Pt_{0.2}Cu_{0.8}$@S-1, the same as $Pt_{0.2}Zn_{0.8}$@S-1. After PDH

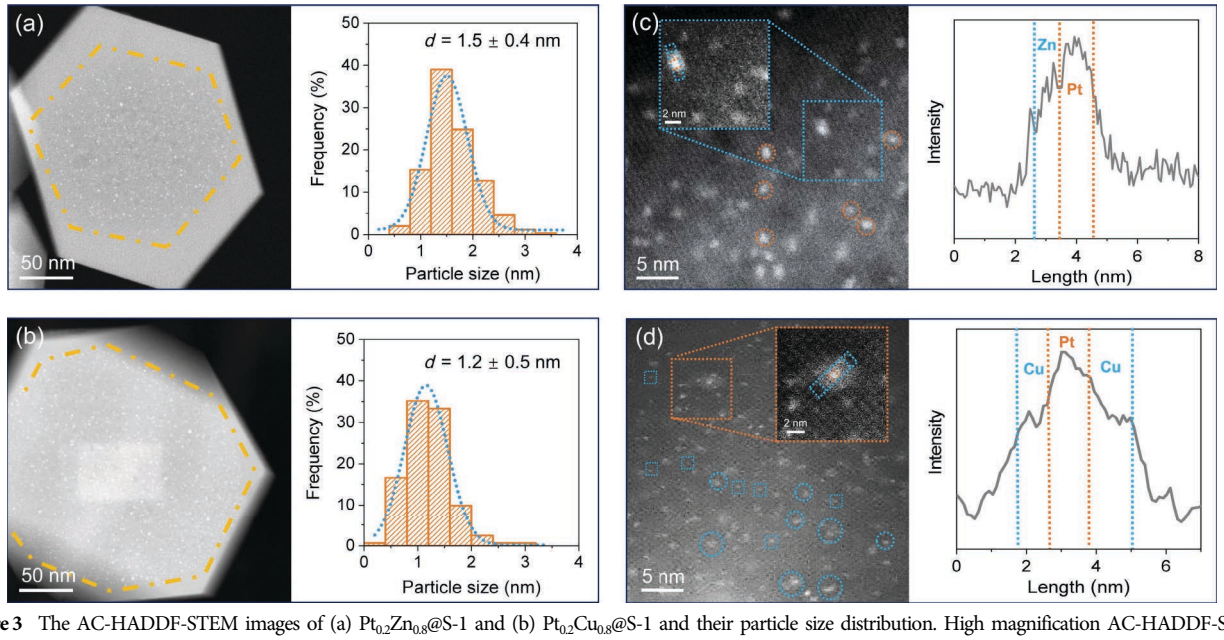


**Figure 3** The AC-HADDF-STEM images of (a) $Pt_{0.2}Zn_{0.8}$@S-1 and (b) $Pt_{0.2}Cu_{0.8}$@S-1 and their particle size distribution. High magnification AC-HADDF-STEM images of bimetallic clusters and the corresponding line profiles taken at the blue rectangles: (c) $Pt_{0.2}Zn_{0.8}$@S-1 and (d) $Pt_{0.2}Cu_{0.8}$@S-1. Pt clusters and SACs are marked in circles and squares, respectively.

reactions, the sizes and compositions of the Pt-based clusters were close to those of the fresh catalysts (Fig. S5 in the ESM), revealing the robust nature of metal@S-1 catalysts.

### 3.2 Chemical state of bimetallic clusters

CO has been widely used as a probe molecule to investigate the local environment state of platinum species [54]. The peak at 2067 $cm^{-1}$ can be ascribed to the CO linear adsorption on the unsaturated metallic Pt sites in $Pt_{0.2}$/S-1 (Fig. 4(a)). This peak shifting to the low wavenumber of 2053 $cm^{-1}$ over $Pt_{0.2}$@S-1 suggested a decrease in Pt size [45, 55]. With the addition of Cu and Zn, this peak further shifted to 2040 and 2026 $cm^{-1}$, respectively, suggesting the formation of bimetallic PtM phases with the chemical decoration of Pt by the second metal. It was reported that the addition of Cu or Zn would transfer electrons to the 5d orbital of Pt and weaken the interaction between Pt and CO molecules, resulting in the redshifts of the CO stretching frequency [56–58].

Infrared spectroscopy can provide elaborate surface hydroxyl information (Fig. 4(b)), based on which we can infer the interaction between PtM and zeolite frameworks [36, 59]. The bands of pristine S-1 in the range of 3750–3716, 3716–3675, and 3640–3610 $cm^{-1}$ can be attributed to the isolated, terminal, and vicinal H-bonded Si–OH groups, respectively [60]. The diversity of Si–OH groups in zeolites may originate from their different locations in twisted zeolite channels and defective zeolite structures [61]. As the loading of Pt and the second metal increased, the intensity of Si–OH groups significantly decreased, indicating that the metal species interact with and consume the Si–OH groups. The ultraviolet–visible diffuse reflectance spectra (UV–vis DRS) also suggest the existence of Si–O–M bonds over reduced $Pt_{0.2}Zn_{0.8}$@S-1 and $Pt_{0.2}Cu_{0.8}$@S-1 catalysts (Fig. S6 in the ESM), i.e., Zn and Cu were in their oxidized state and bonded with S-1 framework. Based on the above, we can infer that the PtM clusters were not fully metallic but partially reduced by $H_2$ and stabilized by the S-1 framework (Fig. 4(b)). This model is similar to the one reported by several other groups [59, 62, 63].

To further analyze the fine chemical structure of the bimetallic PtM clusters inside S-1 crystals, we performed *ex-situ* X-ray absorption near edge structure (XANES) and EXAFS spectra over Pt-based catalysts (Fig. 5). The Pt $L_3$-edge XANES spectra suggest that the Pt species of PtM@S-1 samples were in their low valence state, close to that of Pt foil but not fully reduced (Fig. 5(a)). It is noteworthy that these reduced PtM@S-1 catalysts might be reoxidized by air before *ex-situ* X-ray absorption spectroscopy. Nevertheless, most Pt species of PtM@S-1 in reductive working conditions are expected to be in the metallic state since the reduction temperature of Pt clusters is around 550 °C [37]. The Fourier-transformed EXAFS of the Pt $L_3$-edge was further fitted with Pt–O and Pt–M pathways (Fig. 5(b), and Figs. S7 and S8 and Table S2 in the ESM).

The average coordination numbers (CNs) of Pt–O bonds in $Pt_{0.2}Zn_{0.8}$@S-1, $Pt_{0.2}Cu_{0.8}$@S-1, and $Pt_{0.2}Sn_{1.4}$@S-1 were 2.0, 2.7, and 1.7, respectively, significantly lower than 6 of $PtO_2$. The average CNs of Pt–M (including Pt–Pt and Pt–M) bonds were 2.9, 2.3, and 3.2, respectively, also lower than 12 of Pt foil. These results reveal that the Pt species were partially reduced and stabilized by bonding with the O atoms of the S-1 framework. Besides, the compounding with the second metal could significantly decrease the CNs of Pt–Pt bonds, in other words, increasing the dispersion of Pt species.

Regarding the chemical state of Zn, Sn, and Cu, the X-ray absorption spectroscopy (XAS) spectra evidenced a high valence state, close to that of ZnO, $SnO_2$, and CuO, respectively (Figs. 5(c)–5(f) and Fig. S9 in the ESM). The apparent peak located at $R \approx 1.6$ Å was originated from the first shell Zn–O or Sn–O coordination pathway. In contrast, no Zn–O–Zn ($R \approx 2.9$ Å), Zn–Zn ($R \approx 2.3$ Å), Sn–O–Sn ($R \approx 3.5$ Å), and Sn–Sn ($R \approx 2.8$ Å) coordinations were observed over $Pt_{0.2}Zn_{0.8}$@S-1 and $Pt_{0.2}Sn_{1.4}$@S-1. These results indicate that the second non-noble metal was highly dispersed inside the S-1 framework and stabilized by the Si–O–M bonds. There is no indication of the presence of bulk oxides for these PtM@S-1 catalysts. In summary, we can speculate that for the PtM clusters, Pt species are partially reduced and the second metal is in its oxide state. Pt species are highly dispersed by the second metal with a strong interaction with the S-1 framework.

### 3.3 Propane dehydrogenation

We first evaluated the PDH performances at 550 °C over the Pt- and Pd-based catalysts with the noble metal feeding of 0.75 wt.% in the hydrothermal step. The $Pt_{0.75}$@S-1 already exhibited considerable PDH activity with a $C_3H_8$ conversion of 41% (Fig. 6(a)). However, the $C_3H_6$ selectivity was only 88% with $CH_4$ and $C_2H_6$ as the primary side products, which is unacceptable for PDH reactions. It was reported that the formation of Pt–Pt sites favors the cracking of $C_3H_8$ [39, 64]. Our results partly supported this viewpoint but the segregated Pt clusters do not always catalyze the C–C cleavage. The presence of Pt–Pt sites increased the probability of $C_3H_8$ cracking. With the promotion of Cu, Zn, and Sn, both the $C_3H_8$ conversion and $C_3H_6$ selectivity increased in the order of $Pt_{0.75}Cu_{1.0}$@S-1 < $Pt_{0.75}Zn_{1.0}$@S-1 < $Pt_{0.75}Sn_{1.8}$@S-1. In particular, $Pt_{0.75}Sn_{1.8}$@S-1 offered a high $C_3H_6$ selectivity of 99% at a $C_3H_8$ conversion of 44%, close to the thermodynamic

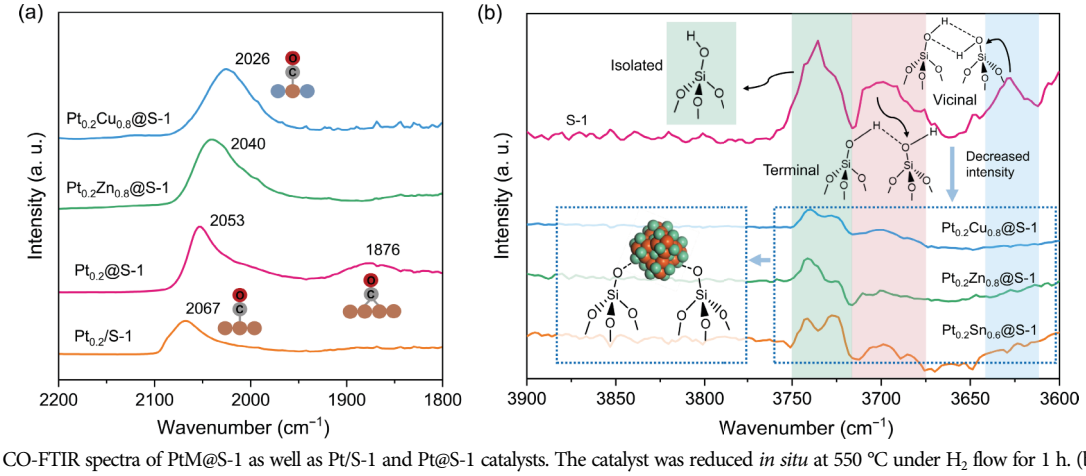


**Figure 4** (a) CO-FTIR spectra of PtM@S-1 as well as Pt/S-1 and Pt@S-1 catalysts. The catalyst was reduced *in situ* at 550 °C under $H_2$ flow for 1 h. (b) IR spectra of PtM@S-1 and pristine S-1 samples in the range of 3900–3600 $cm^{-1}$. The catalyst was activated at 500 °C and vacuumed for 1 h.

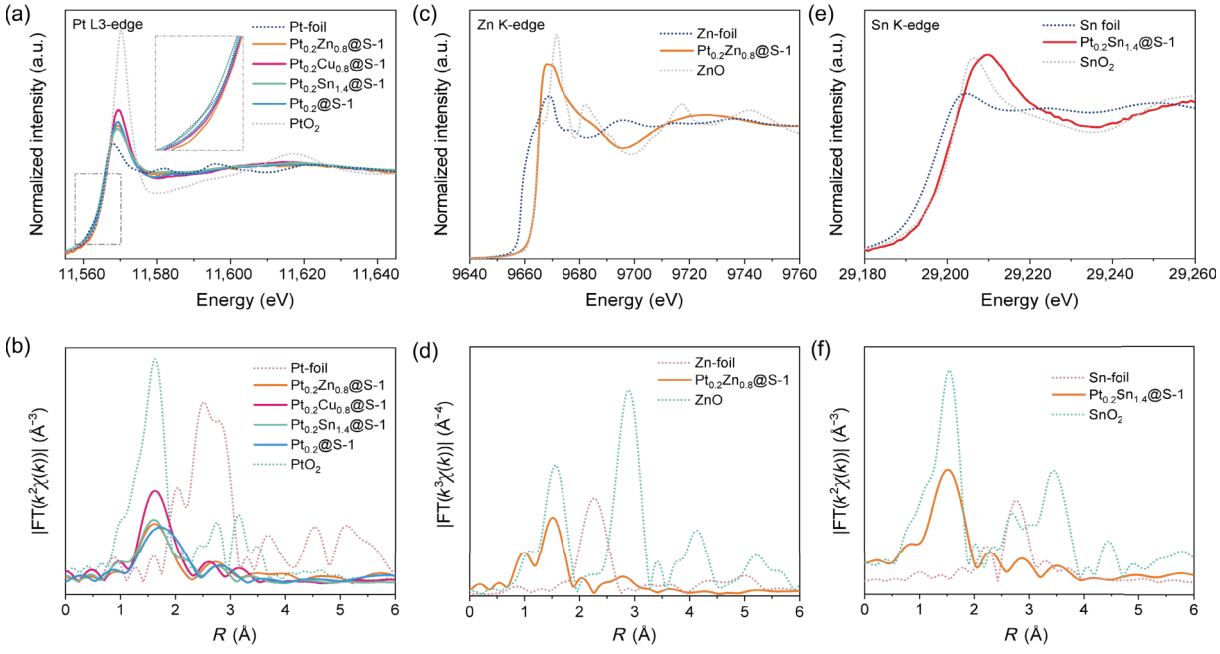


**Figure 5** ((a), (c), and (e)) XANES spectra. The inset shows an enlarged view of pre-edge energy. ((b), (d), and (f)) Fourier transform of $k^2$-weighted EXAFS spectra. Although the samples were pre-reduced, the measurement was performed *ex-situ*. The data are $k^2$- or $k^3$-weighted and not phase corrected.

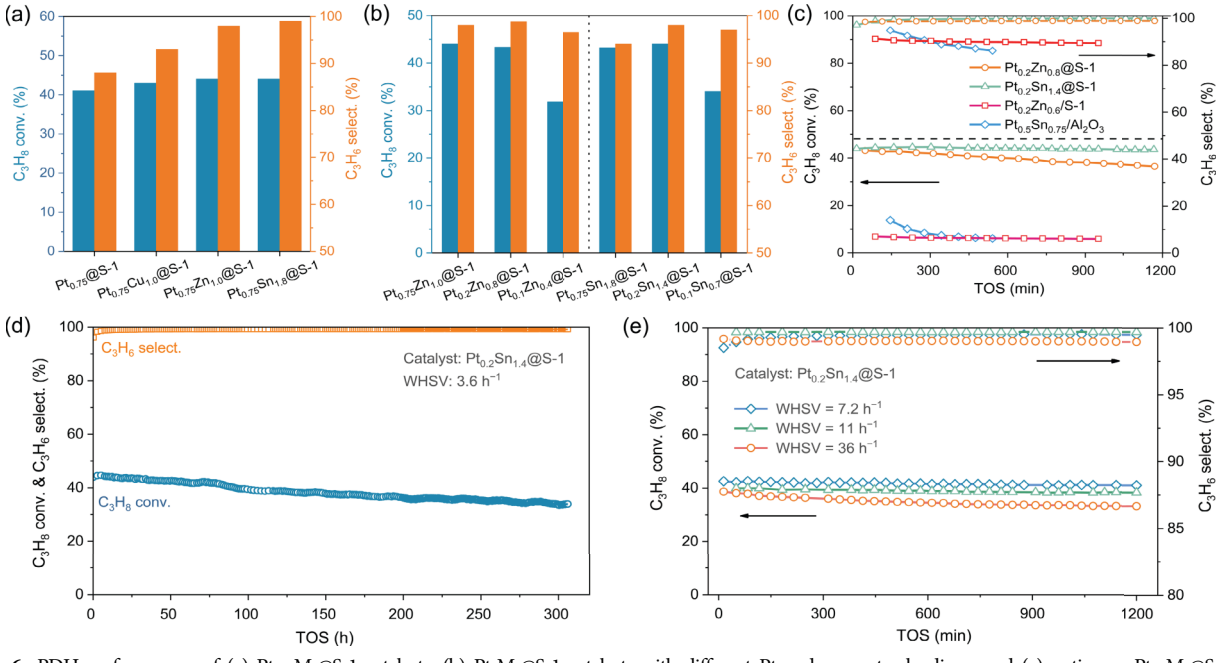


**Figure 6** PDH performances of (a) $Pt_{0.75}M_y$@S-1 catalysts, (b) $Pt_xM_y$@S-1 catalysts with different Pt and promoter loadings, and (c) optimum $Pt_{0.2}M_y$@S-1 and conventional catalysts. (d) Stability and (e) the performances of $Pt_{0.2}Sn_{1.4}$@S-1 under different WHSV. Reaction conditions: $W_{cat}$ = 0.3 g, $C_3H_8$:$N_2$ = 1:3, and $T$ = 550 °C. Detailed reaction conditions and product distributions are listed in Tables S3–S5 in the ESM.

equilibrium of 48%. Considering the high dispersion of bimetallic Pt-based clusters, we can speculate that the decrease of Pt–Pt ensemble sites could minimize the occurrence of C–C cleavage. Although the activity of Pd-based catalysts was lower than that of Pt-based catalysts, the promotion effect of the second metal on Pd-based catalysts was also observed (Fig. S10 in the ESM). These PdM@S-1 catalysts might be applied to methane and $CO_2$ conversions [26, 65].

To make the best of high metal dispersion and confinement structure, we gradually reduced the Pt loading to explore the lower limit for ideal dehydrogenation (Fig. 6(b)). The actual Pt loading was determined by XRF spectrometry (Table S6 in the ESM). The Pt loading of the state-of-the-art commercial $PtSn/Al_2O_3$ catalyst is about 0.3 wt.% [50]. The actual Pt loading of the fresh $Pt_{0.75}Zn_{1.0}$@S-1 catalyst was 0.38 wt.%. Interestingly, the PDH performance in the initial 4 h was not influenced by the Pt loadings in the range of 0.17 wt.%–0.57 wt.% (Tables S4 and S6 in the ESM). An obvious decrease in activity and $C_3H_6$ selectivity was observed over $Pt_{0.1}Zn_{0.4}$@S-1. These results suggest that only a ~ 0.17 wt.% Pt loading for metal@S-1 was sufficient to maintain the PDH reactions.

As another important performance indicator, the catalyst stability was intensively evaluated. The $Pt_{0.5}Sn_{0.75}/Al_2O_3$ catalyst with a 0.5 wt.% Pt loading suffered from fast deactivation (Fig. 6(c)). The $Pt_{0.2}Zn_{0.6}$/S-1 prepared by the impregnation method exhibited low PDH activity. By contrary, the $Pt_{0.2}Sn_{1.4}$@S-1 with only an actual Pt loading of 0.17 wt.% confined in S-1 crystals not only exhibited high $C_3H_8$ conversion levels (45%) and $C_3H_6$ selectivity (99%) but also improved stability, close to their counterparts with high Pt loadings (Table S4 in the ESM).

Therefore, the confinement of PtM clusters inside S-1 crystals could significantly increase the utilization of noble metals.

Under typical PDH reaction conditions with weight hour space velocity ($WHSV_{C_3H_8}$) = 3.6 $h^{-1}$, the $C_3H_8$ conversion only slightly decreased from 45% to 34% after 300 h on stream, and $C_3H_6$ selectivity was stable at 99% (Fig. 6(d)) and the catalyst structure did not change significantly before and after the reaction (Fig. S11 in the ESM). These excellent performance indicators render this catalyst one of the best reported to date (Table S7 in the ESM). The confinement of PtM clusters inside the S-1 crystals allows the catalyst regeneration by a simple calcination step to remove coke and skips the toxic oxychlorination step for redispersing Pt atoms. As expected, the $C_3H_8$ conversion and $C_3H_6$ selectivity of $Pt_{0.2}Sn_{1.4}$@S-1 catalyst could be recovered and sustained after calcination by a 2 vol.% $O_2$ flow at 400 °C (Fig. S12 in the ESM). Furthermore, as the WHSV increased up to 36 $h^{-1}$, the $C_3H_8$ conversion only slightly decreased (Fig. 6(e)), but further increasing the WHSV to 72 $h^{-1}$ led to a $C_3H_8$ conversion lower than 30% (Table S8 in the ESM). Overall, these results suggest the great practicality and stability of metal@S-1 for high-temperature reactions.

## 4 Conclusions

We have synthesized a series of noble metal-based bimetallic clusters confined inside S-1 crystals for PDH reactions. The sizes of these clusters are larger than the micropore sizes of S-1, indicating a collapse of neighboring micropores upon particle growth. The non-noble metal species are hardly reduced, but can highly disperse the noble metal atoms and stabilize the bimetallic clusters by Si–O–M bonds. The Pt-based cluster catalysts, especially PtSn@S-1, PtZn@S-1, and PtCu@S-1, exhibit higher $C_3H_8$ conversion and $C_3H_6$ selectivity than their single-metal counterparts. Because of the high dispersion of noble metals and excellent accessibility, the loading of Pt can be decreased to < 0.2% while keeping a $C_3H_8$ conversion close to the thermodynamic equilibrium and $C_3H_6$ selectivity up to 99%. Furthermore, the optimum PtSn@S-1 catalyst shows superior stability in PDH reaction and high tolerance to calcination for regeneration. This catalyst design strategy might offer new opportunities for the highly efficient utilization of noble metals for heterogeneous catalytic reactions operated under harsh reaction conditions.

## Acknowledgements

This work was supported by the National Key Research and Development Program of the Ministry of Science and Technology (No. 2020YFB0606401), the National Natural Science Foundation of China (Nos. 22222206, 92145301, 22072120, and 12205359), and the Fundamental Research Funds for the Central Universities (Nos. 20720220008 and 20720220021). Specially, we acknowledge the XAFS station (BL14W1) of the Shanghai Synchrotron Radiation Facility for the XAS measurement.

**Electronic Supplementary Material:** Supplementary material (XRD patterns, $N_2$-physisorption, TEM imaging, particle sizes, UV–vis DRS study, XPS spectra, EXAFS fitting, and detailed PDH performances) is available in the online version of this article at https://doi.org/10.1007/s12274-023-5953-y.

## References

[1] Du, Y. X.; Sheng, H. T.; Astruc, D.; Zhu, M. Z. Atomically precise noble metal nanoclusters as efficient catalysts: A bridge between structure and properties. *Chem. Rev.* **2020**, *120*, 526–622.

[2] Zhang, F.; Zeng, M. H.; Yappert, R. D.; Sun, J. K.; Lee, Y. H.; LaPointe, A. M.; Peters, B.; Abu-Omar, M. M.; Scott, S. L. Polyethylene upcycling to long-chain alkylaromatics by tandem hydrogenolysis/aromatization. *Science* **2020**, *370*, 437–441.

[3] Cheng, K.; Smulders, L. C. J.; van Der Wal, L. I.; Oenema, J.; Meeldijk, J. D.; Visser, N. L.; Sunley, G.; Roberts, T.; Xu, Z. R.; Doskocil, E. et al. Maximizing noble metal utilization in solid catalysts by control of nanoparticle location. *Science* **2022**, *377*, 204–208.

[4] Deng, W. P.; Feng, Y. C.; Fu, J.; Guo, H. W.; Guo, Y.; Han, B. X.; Jiang, Z. C.; Kong, L. Z.; Li, C. Z.; Liu, H. C. et al. Catalytic conversion of lignocellulosic biomass into chemicals and fuels. *Green Energy Environ.* **2023**, *8*, 10–114.

[5] Qiao, B. T.; Wang, A. Q.; Yang, X. F.; Allard, L. F.; Jiang, Z.; Cui, Y. T.; Liu, J. Y.; Li, J.; Zhang, T. Single-atom catalysis of CO oxidation using $Pt_1/FeO_x$. *Nat. Chem.* **2011**, *3*, 634–641.

[6] Peng, M.; Dong, C. Y.; Gao, R.; Xiao, D. Q.; Liu, H. Y.; Ma, D. Fully exposed cluster catalyst (FECC): Toward rich surface sites and full atom utilization efficiency. *ACS Cent. Sci.* **2021**, *7*, 262–273.

[7] Dong, C. Y.; Gao, Z. R.; Li, Y. L.; Peng, M.; Wang, M.; Xu, Y.; Li, C. Y.; Xu, M.; Deng, Y. C.; Qin, X. T. et al. Fully exposed palladium cluster catalysts enable hydrogen production from nitrogen heterocycles. *Nat. Catal.* **2022**, *5*, 485–493.

[8] Wang, Y. Q.; Wang, C. T.; Wang, L. X.; Wang, L.; Xiao, F. S. Zeolite fixed metal nanoparticles: New perspective in catalysis. *Acc. Chem. Res.* **2021**, *54*, 2579–2590.

[9] Liu, L. C.; Corma, A. Metal catalysts for heterogeneous catalysis: From single atoms to nanoclusters and nanoparticles. *Chem. Rev.* **2018**, *118*, 4981–5079.

[10] Bartholomew, C. H. Mechanisms of catalyst deactivation. *Appl. Catal. A Gen.* **2001**, *212*, 17–60.

[11] Chen, K.; Li, Y. B.; Wang, M. H.; Wang, Y. H.; Cheng, K.; Zhang, Q. H.; Kang, J. C.; Wang, Y. Functionalized carbon materials in syngas conversion. *Small* **2021**, *17*, 2007527.

[12] Wang, C. T.; Guan, E. J.; Wang, L.; Chu, X. F.; Wu, Z. Y.; Zhang, J.; Yang, Z. Y.; Jiang, Y. W.; Zhang, L.; Meng, X. J. et al. Product selectivity controlled by nanoporous environments in zeolite crystals enveloping rhodium nanoparticle catalysts for $CO_2$ hydrogenation. *J. Am. Chem. Soc.* **2019**, *141*, 8482–8488.

[13] Liu, L. C.; Lopez-Haro, M.; Lopes, C. W.; Li, C. G.; Concepcion, P.; Simonelli, L.; Calvino, J. J.; Corma, A. Regioselective generation and reactivity control of subnanometric platinum clusters in zeolites for high-temperature catalysis. *Nat. Mater.* **2019**, *18*, 866–873.

[14] van Deelen, T. W.; Hernández Mejía, C.; De Jong, K. P. Control of metal–support interactions in heterogeneous catalysts to enhance activity and selectivity. *Nat. Catal.* **2019**, *2*, 955–970.

[15] Deng, S. G.; Lin, Y. S. Sulfur dioxide sorption properties and thermal stability of hydrophobic zeolites. *Ind. Eng. Chem. Res.* **1995**, *34*, 4063–4070.

[16] Zhang, Q.; Yu, J. H.; Corma, A. Applications of zeolites to C1 chemistry: Recent advances, challenges, and opportunities. *Adv. Mater.* **2020**, *32*, 2002927.

[17] Xu, H.; Wu, P. New progress in zeolite synthesis and catalysis. *Natl. Sci. Rev.* **2022**, *9*, nwac045.

[18] Wu, S. M.; Yang, X. Y.; Janiak, C. Confinement effects in zeolite-confined noble metals. *Angew. Chem., Int. Ed.* **2019**, *58*, 12340–12354.

[19] Chen, H.; Li, W.; Zhang, M. C.; Wang, W. Y.; Zhang, X. H.; Lu, F.; Cheng, K.; Zhang, Q. H.; Wang, Y. Boosting propane dehydroaromatization by confining PtZn alloy nanoparticles within H-ZSM-5 crystals. *Catal. Sci. Technol.* **2022**, *12*, 7281–7292.

[20] Yang, Z. Y.; Li, H.; Zhou, H.; Wang, L.; Wang, L. X.; Zhu, Q. Y.; Xiao, J. P.; Meng, X. J.; Chen, J. X.; Xiao, F. S. Coking-resistant iron catalyst in ethane dehydrogenation achieved through siliceous zeolite modulation. *J. Am. Chem. Soc.* **2020**, *142*, 16429–16436.

[21] Li, K. H.; Valla, J.; Garcia-Martinez, J. Realizing the commercial potential of hierarchical zeolites: New opportunities in catalytic cracking. *ChemCatChem* **2014**, *6*, 46–66.

[22] Cheng, K.; van Der Wal, L. I.; Yoshida, H.; Oenema, J.; Harmel, J.; Zhang, Z.; Sunley, G.; Zečević, J.; De Jong, K. P. Impact of the spatial organization of bifunctional Metal-Zeolite catalysts on the hydroisomerization of light alkanes. *Angew. Chem., Int. Ed.* **2020**, *59*, 3592–3600.

[23] Chai, Y. C.; Qin, B.; Li, B. N.; Dai, W. L.; Wu, G. J.; Guan, N. J.; Li, L. D. Zeolite-encaged mononuclear copper centers catalyze $CO_2$ selective hydrogenation to methanol. *Natl. Sci. Rev.*, in press, https://doi.org/10.1093/nsr/nwad043.
[24] Kistler, J. D.; Chotigkrai, N.; Xu, P. H.; Enderle, B.; Praserthdam, P.; Chen, C. Y.; Browning, N. D.; Gates, B. C. A single-site platinum CO oxidation catalyst in zeolite KLTL: Microscopic and spectroscopic determination of the locations of the Platinum atoms. *Angew. Chem., Int. Ed.* **2014**, *53*, 8904–8907.
[25] Li, Y.; Yu, J. H. Emerging applications of zeolites in catalysis, separation and host–guest assembly. *Nat. Rev. Mater.* **2021**, *6*, 1156–1174.
[26] Wang, W. Y.; Zhou, W.; Li, W.; Xiong, X. W.; Wang, Y. H.; Cheng, K.; Kang, J. C.; Zhang, Q. H.; Wang, Y. *In-situ* confinement of ultrasmall palladium nanoparticles in silicalite-1 for methane combustion with excellent activity and hydrothermal stability. *Appl. Catal. B: Environ.* **2020**, *276*, 119142.
[27] Hughes, A. E.; Haque, N.; Northey, S. A.; Giddey, S. Platinum group metals: A review of resources, production and usage with a focus on catalysts. *Resources* **2021**, *10*, 93.
[28] Regali, F.; Liotta, L. F.; Venezia, A. M.; Boutonnet, M.; Järås, S. Hydroconversion of n-hexadecane on Pt/silica-alumina catalysts: Effect of metal loading and support acidity on bifunctional and hydrogenolytic activity. *Appl. Catal. A: Gen.* **2014**, *469*, 328–339.
[29] Li, Z.; Ji, S. F.; Liu, Y. W.; Cao, X.; Tian, S. B.; Chen, Y. J.; Niu, Z. Q.; Li, Y. D. Well-defined materials for heterogeneous catalysis: From nanoparticles to isolated single-atom sites. *Chem. Rev.* **2020**, *120*, 623–682.
[30] Jin, Z.; Wang, L.; Zuidema, E.; Mondal, K.; Zhang, M.; Zhang, J.; Wang, C. T.; Meng, X. J.; Yang, H. Q.; Mesters, C. et al. Hydrophobic zeolite modification for *in situ* peroxide formation in methane oxidation to methanol. *Science* **2020**, *367*, 193–197.
[31] Zhang, Q.; Gao, S. Q.; Yu, J. H. Metal sites in zeolites: Synthesis, characterization, and catalysis. *Chem. Rev.* **2023**, *123*, 6039–6106.
[32] Wang, N.; Sun, Q. M.; Yu, J. H. Ultrasmall metal nanoparticles confined within crystalline nanoporous materials: A fascinating class of nanocatalysts. *Adv. Mater.* **2019**, *31*, 1803966.
[33] Liu, Y. T.; Zhang, L. F.; Dong, Z. J.; Luo, L. L. Precise control of Pt encapsulation in zeolite-based catalysts for a stable low-temperature CO oxidation reaction. *Sci. China Chem.* **2022**, *65*, 2015–2022.
[34] Konnov, S. V.; Dubray, F.; Clatworthy, E. B.; Kouvatas, C.; Gilson, J. P.; Dath, J. P.; Minoux, D.; Aquino, C.; Valtchev, V.; Moldovan, S. et al. Novel strategy for the synthesis of ultra-stable single-site Mo-ZSM-5 zeolite nanocrystals. *Angew. Chem., Int. Ed.* **2020**, *59*, 19553–19560.
[35] Motagamwala, A. H.; Almallahi, R.; Wortman, J.; Igenegbai, V. O.; Linic, S. Stable and selective catalysts for propane dehydrogenation operating at thermodynamic limit. *Science* **2021**, *373*, 217–222.
[36] Zhao, D.; Tian, X. X.; Doronkin, D. E.; Han, S. L.; Kondratenko, V. A.; Grunwaldt, J. D.; Perechodjuk, A.; Vuong, T. H.; Rabeah, J.; Eckelt, R. et al. *In situ* formation of $ZnO_x$ species for efficient propane dehydrogenation. *Nature* **2021**, *599*, 234–238.
[37] Wang, P.; Yang, M.; Liao, H. F.; Xu, K. Y.; Zong, X. P.; Xie, Z. L.; Zhao, H. B.; Xu, Y. J.; Yang, H.; Gan, Y. Y. et al. Restructured zeolites anchoring singly dispersed bimetallic platinum and zinc catalysts for propane dehydrogenation. *Cell Rep. Phys. Sci.* **2023**, *4*, 101311.
[38] Wang, P.; Yao, J. K.; Jiang, Q. K.; Gao, X. H.; Lin, D.; Yang, H.; Wu, L. Z.; Tang, Y.; Tan, L. Stabilizing the isolated Pt sites on $PtGa/Al_2O_3$ catalyst via silica coating layers for propane dehydrogenation at low temperature. *Appl. Catal. B:Environ.* **2022**, *300*, 120731.
[39] Monai, M.; Gambino, M.; Wannakao, S.; Weckhuysen, B. M. Propane to olefins tandem catalysis: A selective route towards light olefins production. *Chem. Soc. Rev.* **2021**, *50*, 11503–11529.
[40] Dai, Y. H.; Gao, X.; Wang, Q. J.; Wan, X. Y.; Zhou, C. M.; Yang, Y. H. Recent progress in heterogeneous metal and metal oxide catalysts for direct dehydrogenation of ethane and propane. *Chem. Soc. Rev.* **2021**, *50*, 5590–5630.
[41] Shi, L.; Deng, G. M.; Li, W. C.; Miao, S.; Wang, Q. N.; Zhang, W. P.; Lu, A. H. $Al_2O_3$ Nanosheets rich in pentacoordinate $Al^{3+}$ ions stabilize Pt-Sn clusters for propane dehydrogenation. *Angew. Chem., Int. Ed.* **2015**, *54*, 13994–13998.
[42] Perechodjuk, A.; Zhang, Y. Y.; Kondratenko, V. A.; Rodemerck, U.; Linke, D.; Bartling, S.; Kreyenschulte, C. R.; Jiang, G. Y.; Kondratenko, E. V. The effect of supported Rh, Ru, Pt or Ir nanoparticles on activity and selectivity of $ZrO_2$-based catalysts in non-oxidative dehydrogenation of propane. *Appl. Catal. A: Gen.* **2020**, *602*, 117731.
[43] Rochlitz, L.; Pessemesse, Q.; Fischer, J. W. A.; Klose, D.; Clark, A. H.; Plodinec, M.; Jeschke, G.; Payard, P. A.; Copéret, C. A robust and efficient propane dehydrogenation catalyst from unexpectedly segregated $Pt_2Mn$ nanoparticles. *J. Am. Chem. Soc.* **2022**, *144*, 13384–13393.
[44] Liu, L. C.; Díaz, U.; Arenal, R.; Agostini, G.; Concepción, P.; Corma, A. Generation of subnanometric platinum with high stability during transformation of a 2D zeolite into 3D. *Nat. Mater.* **2017**, *16*, 132–138.
[45] Sun, Q. M.; Wang, N.; Fan, Q. Y.; Zeng, L.; Mayoral, A.; Miao, S.; Yang, R. O.; Jiang, Z.; Zhou, W.; Zhang, J. C. et al. Subnanometer bimetallic platinum-zinc clusters in zeolites for propane dehydrogenation. *Angew. Chem., Int. Ed.* **2020**, *59*, 19450–19459.
[46] Zhou, J.; Liu, H.; Xiong, C.; Hu, P.; Wang, H.; Wang, X. Y.; Ji, H. B. Potassium-promoted Pt-In bimetallic clusters encapsulated in silicalite-1 zeolite for efficient propane dehydrogenation. *Chem. Eng. J.* **2023**, *455*, 139794.
[47] Zhang, W. Q.; Zhang, X. B.; Wang, J. Y.; Ghosh, A.; Zhu, J.; LiBretto, N. J.; Zhang, G. H.; Datye, A. K.; Liu, W.; Miller, J. T. Bismuth-modulated surface structural evolution of $Pd_3Bi$ intermetallic alloy catalysts for selective propane dehydrogenation and acetylene semihydrogenation. *ACS Catal.* **2022**, *12*, 10531–10545.
[48] Zhou, Y. L.; Wei, F. F.; Qi, H. F.; Chai, Y. C.; Cao, L. R.; Lin, J.; Wan, Q.; Liu, X. Y.; Xing, Y. N.; Lin, S. et al. Peripheral-nitrogen effects on the Ru1 centre for highly efficient propane dehydrogenation. *Nat. Catal.* **2022**, *5*, 1145–1156.
[49] Zeng, L.; Li, W.; Wei, X. E.; Cheng, J. W.; Zhou, W.; Zheng, Y. P.; Cai, F.; Liu, Y. F.; Cheng, K.; Zhang, Q. H. et al. IrGa bimetallic catalyst with atomical metal dispersion for propane dehydrogenation with high stability. *ChemCatChem* **2023**, *15*, e202201405.
[50] Chen, S.; Zhao, Z. J.; Mu, R. T.; Chang, X.; Luo, J.; Purdy, S. C.; Kropf, A. J.; Sun, G. D.; Pei, C. L.; Miller, J. T. et al. Propane dehydrogenation on single-site $[PtZn_4]$ intermetallic catalysts. *Chem* **2021**, *7*, 387–405.
[51] Newville, M. IFEFFIT: Interactive XAFS analysis and FEFF fitting. *J. Synchrotron. Radiat.* **2001**, *8*, 322–324.
[52] Friedrich, H.; De Jongh, P. E.; Verkleij, A. J.; De Jong, K. P. Electron tomography for heterogeneous catalysts and related nanostructured materials. *Chem. Rev.* **2009**, *109*, 1613–1629.
[53] Zečević, J.; van Der Eerden, A. M. J.; Friedrich, H.; De Jongh, P. E.; De Jong, K. P. Heterogeneities of the nanostructure of Platinum/zeolite Y catalysts revealed by electron tomography. *ACS Nano* **2013**, *7*, 3698–3705.
[54] Zhang, B. F.; Li, G. Z.; Zhai, Z. W.; Chen, D. L.; Tian, Y. J.; Yang, R. O.; Wang, L.; Zhang, X. W.; Liu, G. Z. PtZn intermetallic nanoalloy encapsulated in silicalite-1 for propane dehydrogenation. *AIChE J.* **2021**, *67*, e17295.
[55] Kappers, M. J.; Van Der Maas, J. H. Correlation between CO frequency and Pt coordination number. A DRIFT study on supported Pt catalysts. *Catal. Lett.* **1991**, *10*, 365–373.
[56] Yu, C. L.; Xu, H. Y.; Ge, Q. J.; Li, W. Z. Properties of the metallic phase of zinc-doped platinum catalysts for propane dehydrogenation. *J. Mol. Catal. A: Chem.* **2007**, *266*, 80–87.
[57] Sun, G. D.; Zhao, Z. J.; Mu, R. T.; Zha, S.; Li, L. L.; Chen, S.; Zang, K. T.; Luo, J.; Li, Z. L.; Purdy, S. C. et al. Breaking the scaling relationship via thermally stable Pt/Cu single atom alloys for catalytic dehydrogenation. *Nat. Commun.* **2018**, *9*, 4454.
[58] Ma, Y.; Chen, X.; Guan, Y. J.; Xu, H.; Zhang, J. W.; Jiang, J. G.; Chen, L.; Xue, T.; Xue, Q. S.; Wei, F. et al. Skeleton-Sn anchoring isolated Pt site to confine subnanometric clusters within *BEA topology. *J. Catal.* **2021**, *397*, 44–57.
[59] Qi, L.; Babucci, M.; Zhang, Y. F.; Lund, A.; Liu, L. M.; Li, J. W.;

Chen, Y. Z.; Hoffman, A. S.; Bare, S. R.; Han, Y. et al. Propane dehydrogenation catalyzed by isolated Pt atoms in ≡SiOZn-OH nests in dealuminated zeolite beta. *J. Am. Chem. Soc.* **2021**, *143*, 21364–21378.

[60] Omegna, A.; Vasic, M.; Anton van Bokhoven, J.; Pirngruber, G.; Prins, R. Dealumination and realumination of microcrystalline zeolite beta: An XRD, FTIR and quantitative multinuclear (MQ) MAS NMR study. *Phys. Chem. Chem. Phys.* **2004**, *6*, 447–452.

[61] Janiszewska, E.; Macario, A.; Wilk, J.; Aloise, A.; Kowalak, S.; Nagy, J. B.; Giordano, G. The role of the defect groups on the silicalite-1 zeolite catalytic behavior. *Micropor. Mesopor. Mater.* **2013**, *182*, 220–228.

[62] Song, M. X.; Zhang, B. F.; Zhai, Z. W.; Liu, S. B.; Wang, L.; Liu, G. Z. Highly dispersed Pt stabilized by $ZnO_x$-Si on self-pillared zeolite nanosheets for propane dehydrogenation. *Ind. Eng. Chem. Res.* **2023**, *62*, 3853–3861.

[63] Zhang, T. T.; Pei, C. L.; Sun, G. D.; Chen, S.; Zhao, Z. J.; Sun, S. J.; Lu, Z. P.; Xu, Y. Y.; Gong, J. L. Synergistic mechanism of platinum-$GaO_x$ catalysts for propane dehydrogenation. *Angew. Chem., Int. Ed.* **2022**, *61*, e202201453.

[64] Lian, Z.; Ali, S.; Liu, T. F.; Si, C. W.; Li, B.; Su, D. S. Revealing the Janus character of the coke precursor in the propane direct dehydrogenation on Pt catalysts from a kMC simulation. *ACS Catal.* **2018**, *8*, 4694–4704.

[65] Zhang, F. Y.; Zhou, W.; Xiong, X. W.; Wang, Y. H.; Cheng, K.; Kang, J. C.; Zhang, Q. H.; Wang, Y. Selective hydrogenation of $CO_2$ to ethanol over sodium-modified rhodium nanoparticles embedded in zeolite silicalite-1. *J. Phys. Chem. C* **2021**, *125*, 24429–24439.